NJC

ROYAL SOCIETY OF CHEMISTRY

PAPER

Check for updates

Cite this: *New J. Chem.*, 2020, **44**, 2210

Co(II) and Zn(II) pyrazolyl-benzimidazole complexes with remarkable antibacterial activity†

Karim Chkirate,[a] Khalid Karrouchi,[b] Necmi Dege,[c] Nada Kheira Sebbar,[ad] Abdelaziz Ejjoummany,[e] Smaail Radi,[f] N. N. Adarsh,[g] Ahmed Talbaoui,[h] Marilena Ferbinteanu,[i] El Mokhtar Essassi[a] and Yann Garcia *[g]

Received 27th November 2019,
Accepted 2nd January 2020

DOI: 10.1039/c9nj05913j

rsc.li/njc

Three mononuclear coordination complexes of 1-butyl-2-((5-methyl-1*H*-pyrazol-3-yl)methyl)-1*H*-benzimidazole (**L**), namely $[CoL]Cl_2$ (**C1**), $[Co_2L_2]Cl_2{\cdot}H_2O$ (**C2**) and $[Zn_2L_2]Cl_2$ (**C3**), have been synthesized and characterized spectroscopically. Their single-crystal X-ray diffraction analysis revealed that **C1** and **C2** display pseudopolymorphism. The presence of N–H···Cl and C–H···Cl hydrogen bonding in the crystal structure of **C1** and **C3** assists the formation of a 2D hydrogen bonded sheet and orthogonal packing [2D sheet + a pair of 1D chains], respectively, leading to supramolecular structures. A combination of N–H···Cl, C–H···Cl, O–H···Cl, and C–H···O interactions results however in a 2D corrugated hydrogen bonded sheet with inclusion of water molecules in **C2**. Hirshfeld surface analysis confirms that hydrogen bonding and π-stacking contacts stabilize the crystal structures. These metal complexes display good performance towards their antimicrobial activity against *Escherichia coli, Pseudomonas aeruginosa*, and *Staphylococcus aureus*. In particular a normalized minimum inhibitory concentration as low as 6.25 μg mL^{-1} for the bacterial strains was recorded for **C2**. Its structure–bioactivity correlation is discussed in detail.

Introduction

Nitrogen based ligands have attracted more attention in recent years due to their interesting properties, *e.g.* in bio-inorganic and structural chemistry,[1,2] spin crossover research,[3,4] and molecular magnetism.[5] This ability is mainly due to the presence of sp^2 hybridized nitrogen donors,[6] with the involvement in some cases of other sites such as donating oxygen and sulfur atoms.[7] Among these molecules, azole based molecules, in particular pyrazoles and benzimidazoles, are present in many pharmaceuticals, covering a wide range of biological properties.[8–11] Their derivatives display important anti-cancer activities, inhibiting the proliferation of human tumor cells.[12,13]

The ability of benzimidazole derivatives to form stable complexes with metal ions gives rise to various modes of metal–ligand coordination.[14] Other studies have explored the biological activity of coordination compounds containing the benzimidazole moiety.[15] Benzimidazole coordination complexes have relatively high antibacterial and antifungal properties.[16] Their zinc complexes, in addition to their antimicrobial activity, have been used in anti-cancer studies *in vitro* and *in vivo* and have been shown to play an important role in the chemotherapeutic process.[17] With other metals, these derivatives exerted significant cytotoxic activity.[13,18,19]

While their ruthenium(II) and europium(III) complexes display luminescent properties,[20,21] whereas their Fe(II) complexes display spin crossover behaviour,[22] Zn(II), Ni(II), Co(II) and Cu(II) complexes have been studied for their alkaline phosphatase (ALP) inhibition activities, their antioxidant potential, and their antimicrobial activities.[23] On the other hand, pyrazole metal complexes have proven antimicrobial activities,[24] as well as applications in catalysis,[25] and molecular electronics.[26]

In order to search for new ligand candidates for assembly of metal complexes, we considered to use in the same platform both pyrazolyl and benzimidazole units. This strategy has proved

[a] *Laboratory of Heterocyclic Organic Chemistry, Department of Chemistry, Faculty of Sciences, Mohamed V University, BP1014, Rabat, 10100, Morocco*
[b] *Laboratory of Medicinal Chemistry, Faculty of Medicine and Pharmacy, University Mohammed V, Rabat, Morocco*
[c] *Ondokuz Mayıs University, Faculty of Arts and Sciences, Department of Physics, 55139, Kurupelit, Samsun, Turkey*
[d] *Laboratoire de Chimie Appliquée et Environnement, Equipe de Chimie Bioorganique Appliquée, Faculté des Sciences, Université Ibn Zohr, Agadir, Morocco*
[e] *Laboratoire de Chimie Physique et Chimie Bioorganique, FST Mohammedia, Université Hassan II de Casablanca, BP 146, 28800, Mohammedia, Morocco*
[f] *LCAE, Département de Chimie, Faculté des Sciences, Université Mohamed I, BP 524, 60 000 Oujda, Morocco*
[g] *Institute of Condensed Matter and Nanosciences, Molecular Chemistry, Materials and Catalysis (IMCN/MOST), Université Catholique de Louvain, Place L. Pasteur 1, 1348 Louvain-la-Neuve, Belgium. E-mail: yann.garcia@uclouvain.be*
[h] *Laboratoire de Biologie des Pathologies Humaines, Faculté des Sciences, Université Mohammed V, Rabat, Morocco*
[i] *Inorganic Chemistry Department, Faculty of Chemistry, University of Bucharest, Dumbrava Rosie 23, Bucharest 020462, Romania*

† Electronic supplementary information (ESI) available. CCDC 1895214, 1895673 and 1959576. For ESI and crystallographic data in CIF or other electronic format see DOI: 10.1039/c9nj05913j

 This journal is © The Royal Society of Chemistry and the Centre National de la Recherche Scientifique 2020

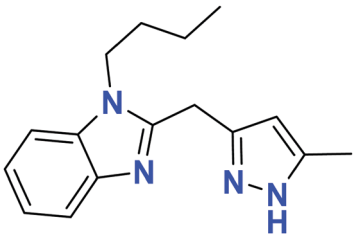

Scheme 1 1-Butyl-2-((5-methyl-1*H*-pyrazol-3-yl)methyl)-1*H*-benzimidazole (**L**).

to be recently successful with the design of a bifunctional ligand combining 1,2,4-triazolyl and tetrazole units, to afford a multi-coloured sensor.[27] Such dissymmetric molecules are particularly interesting as ligands for the construction of polynuclear complexes as well as models for bioinorganic systems.[28–31] Continuing our research along this line,[32–36] we have designed a new benzimidazole derivative functionalized with a pyrazole unit leading to **L**, namely 1-*n*-butyl-2-((5-methyl-1*H*-pyrazol-3-yl)methyl)-1*H*-benzimidazole (Scheme 1). We were recently intrigued by a recent report that suggested a crystal structure–bioactivity correlation: crystalline materials having lattice included water molecules would have more antibacterial activity, due to the hydrophilic attraction of the bacterial cell wall.[37] Stimulated by this discovery, we have applied a new design approach by reacting the new ligand **L** with $CoCl_2{\cdot}6H_2O$ or $ZnCl_2$. We have used either pure EtOH or a mixture of EtOH and water, in order to favour the inclusion of water in our complexes, and establish a comparison with a non hydrated material. The crystal structures of three novel Co(II) and Zn(II) coordination complexes **C1–C3** obtained from these reaction conditions are discussed. In addition, the antibacterial activities of **L** and its precursors **3** and **4**, as well as for the complexes **C1–C3**, were evaluated against Gram-positive and Gram-negative bacteria such as *Staphylococcus aureus*, *Escherichia coli* and *Pseudomonas aeruginosa*.

Results

Synthesis of L

We have developed a simple, high-throughput synthesis procedure in a few steps in order to prepare the desired pyrazolyl-benzimidazole derivative (**L**) (Scheme 2). The majority product **3**[35] was produced in good yield by condensation of *o*-phenylenediamine with dehydroacetic acid (DHA) under reflux in xylene for 4 h. The second step consisted of reacting **3** with 1-bromobutane under the conditions of liquid–liquid phase transfer catalysis with stirring at room temperature for 48 h to give the alkylated 1,5-benzodiazepine **4** in satisfactory yield. The third step was to react an excess of hydrazine monohydrate with **4** in refluxing ethanol for 2 h to afford the pyrazolyl-benzimidazole molecule **L** in good yield (Scheme 2).

Synthesis of coordination complexes C1, C2 and C3

Crystallization of the coordination compounds was obtained by reaction of the pyrazolyl-benzimidazole ligand **L** and Co(II), on one hand in an ethanolic solution (M : L/1 : 1) and on the other hand in an aqueous ethanolic solution (M : L/1 : 1). Reaction of the ligand **L** with Zn(II) in an ethanolic solution (M : L/1 : 1) was also carried out. These syntheses led to single crystals of three coordination complexes whose formula was established by X-ray diffraction and mass spectrometry: $[Co\mathbf{L}]Cl_2$ (**C1**), $[Co_2\mathbf{L}_2]Cl_2{\cdot}H_2O$ (**C2**) and $[Zn_2\mathbf{L}_2]Cl_2$ (**C3**).

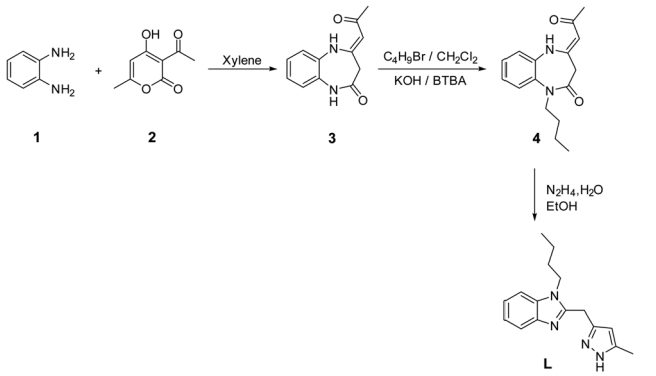

Scheme 2 Synthetic route of L.

X-ray crystallography

The coordination complexes **C1–C3** are mononuclear coordination complexes derived from **L** and Co(II)/Zn(II), which crystallize in the monoclinic $P2_1/c$, triclinic $P\bar{1}$, and monoclinic $C2/c$ space groups, respectively (Table 1). From the single crystal X-ray diffraction data analysis, **C1** and **C2** are identified as pseudopolymorphs, *i.e.* they only differ in the presence of a solvent water molecule, the number of molecules per asymmetric unit, and their space group. While the central metal ions in **C1** and **C2** are Co(II), the central metal ion in **C3** is Zn(II). In the crystal structure, **C2** exists in monohydrated form (Fig. 1).

Crystal structure of C1

Blue coloured prism shaped single crystals of **C1** were obtained by slow evaporation of the mixture of ligand **L** and $CoCl_2{\cdot}2H_2O$ (1 : 1 stoichiometric ratio) in EtOH. They crystallized in a monoclinic centrosymmetric space group $P2_1/c$ (Table 1). The asymmetric unit of **C1** consists of a molecule of the Co(II) coordination complex of **L**, and two chloride anions. The Co(II) metal centre showed distorted tetrahedral geometry [$\angle$N–Co–N = 92.38(11)°; $\angle$N–Co–Cl = 109.18(9)–116.49(8)°; $\angle$Cl–Co–Cl = 111.38(4)°] in which the coordination sites are occupied by two chloride anions, and N atoms of imidazole and pyrazole of the ligand **L**.

Four such molecules were present in the unit cell (Fig. S1, ESI†), and they are symmetrically related by a glide plane, centre of inversion and 2-fold screw axis. The ligand molecule showed non-planarity as expected due to the presence of the $-CH_2-$ spacer between the imidazole and pyrazole functionalities (the torsion angle between the planes of the imidazole and pyrazole ring is ~12.71°). The Co(II) mononuclear complex **C1** exhibits C–H···Cl hydrogen bonding [C–H···Cl = 3.653(3) Å, $\angle$C–H–Cl = 155°] involving the C–H of the $-CH_2-$ spacer and

Table 1 Crystal data of **C1**, **C2** and **C3**

Crystal data	C1	C2	C3
Empirical formula	$C_{16}H_{20}Cl_2CoN_4$	$C_{32}H_{42}Cl_4Co_2N_8O$	$C_{16}H_{20}Cl_2N_4Zn$
CCDC	1895214	1959576	1895673
Formula weight	398.19	814.39	404.63
Crystal size (mm)	0.72 × 0.44 × 0.29	0.40 × 0.25 × 0.07	0.48 × 0.31 × 0.11
Crystal system	Monoclinic	Triclinic	Monoclinic
Space group	$P2_1/c$	$P\bar{1}$	$C2/c$
a (Å)	10.6315(8)	8.7970(15)	21.6975(12)
b (Å)	9.9746(5)	11.744(2)	8.4668(3)
c (Å)	16.8984(13)	19.603(4)	40.556(2)
α (°)	90.000	77.180(5)	90.000
β (°)	90.076(6)	82.835(6)	102.999(4)
γ (°)	90.000	74.748(5)	90.000
Volume (Å^3)	1792.0(2)	1900.4(6)	7259.5(6)
Z	4	2	16
$D_{calc.}$ (g cm^{-3})	1.476	1.423	1.481
F(000)	820	840	3328
μMoKα (mm^{-1})	1.259	1.191	1.651
T (K)	296(2)	293(2)	293(2)
Range of h, k, l	−12/13, −12/10, −20/20	−11/10, −15/15, −25/25	−19/25, −8/9, −46/46
θ min/max	1.916/25.998	3.047/27.485	1.031/24.417
Reflections collected/unique/observed	14 397/3522/2061	26 606/8569/4355	17 227/5922/3724
Data/restraints/parameters	3522/0/210	8569/2/427	5922/0/419
Goodness of fit on F^2	0.874	1.051	0.895
Final R indices [$I > 2\sigma(I)$]	R_1 = 0.0397, wR_2 = 0.0712	R_1 = 0.1230, wR_2 = 0.2922	R_1 = 0.0454, wR_2 = 0.1072
R indices (all data)	R_1 = 0.0889, wR_2 = 0.0808	R_1 = 0.2007, wR_2 = 0.3389	R_1 = 0.0773, wR_2 = 0.1187

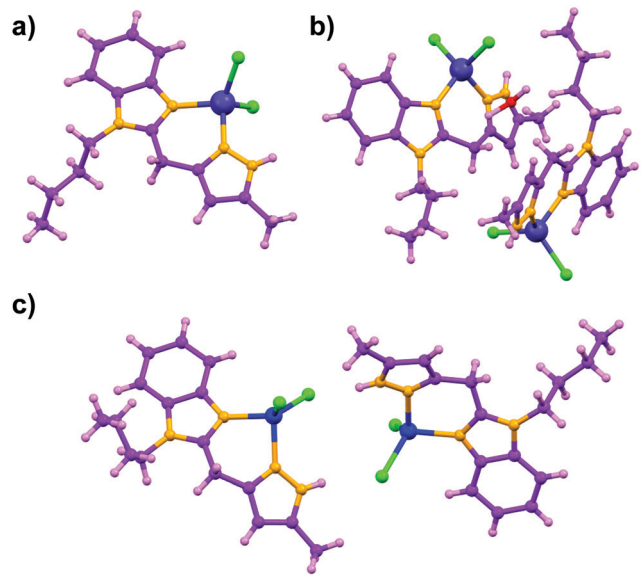

Fig. 1 Asymmetric unit of **C1** (a), **C2** (b), and **C3** (c). Colour codes: C – purple, N – orange, H – light purple, Co/Zn – blue, O – red, Cl – green.

the metal bound chloride anion. Such hydrogen bonding resulted in the formation of a zero dimensional (0D) hydrogen bonded macrocycle. Interestingly such macrocycles undergo further hydrogen bonding through N–H···Cl [N–H···Cl = 3.253(3) Å, ∠N–H–Cl = 149°] having the N–H of pyrazole and metal bound chloride anion, which resulted in the formation of a two dimensional (2D) hydrogen bonded sheet structure. These 2D sheets are packed in a parallel fashion with the support of a C–H···π interaction [3.586 Å] involving –CH_3 of the butyl side chain, and C–H···Cl hydrogen bonding *via* –CH_2– of the butyl side chain and the metal coordinated chloride anion [C–H···Cl = 3.858(4) Å, ∠C–H–Cl = 168.31°] (Fig. 2).

Crystal structure C2

The reaction of ligand L and $CoCl_2{\cdot}2H_2O$ (1 : 1 stoichiometric ratio) in EtOH and water (1 : 1 v/v) resulted in blue coloured prism shaped single crystals of **C2**. Single crystal X-ray diffraction analysis of **C2** revealed the formation of a solvent induced pseudopolymorph of **C1**. The single crystals of **C2** belong to triclinic centrosymmetric space group $P\bar{1}$. The asymmetric unit comprises two molecules of the Co(II) coordination complex of L, four chloride anions (two are coordinated to each Co(II)), and a water molecule (guest solvent). In the unit cell, two such units are present and are symmetrically related by an inversion centre (Fig. S2, ESI†). The Co(II) metal centre showed distorted tetrahedral geometry [∠N–Co–N = 91.5(3)–91.7(3)°; ∠N–Co–Cl = 108.0(3)–115.9(3)°; ∠Cl–Co–Cl = 113.67(13)–113.87(12)°] in which the coordination sites are occupied by two chloride anions, and N atoms of imidazole and pyrazole of the ligand L. The ligand L exhibited nonplanar geometry, confirmed by the torsion angle (14.35 and 32.24° for crystallographically independent complexes) between the planes of the imidazole and pyrazole functionalities. The crystallographically independent molecules of the Co(II) complex recognize each other through N–H···Cl hydrogen bonding [N–H···Cl = 3.203(10)–3.374(8) Å, ∠N–H–Cl = 160–176°] involving the N–H of the pyrazole and metal coordinated chloride anion, resulting in a 0D hydrogen bonded synthon. This synthon further undergoes self-assembly *via* O–H···Cl [O–H···Cl = 3.179(17) Å, ∠O–H–Cl = 138°], C–H···Cl [C–H···Cl = 3.624(15)–3.71(3) Å, ∠C–H–Cl = 149–159°] and C–H···O [C–H···O = 3.09(3) Å, ∠C–H–O = 139°] hydrogen bonding involving lattice included water with the chloride anion,

 This journal is © The Royal Society of Chemistry and the Centre National de la Recherche Scientifique 2020

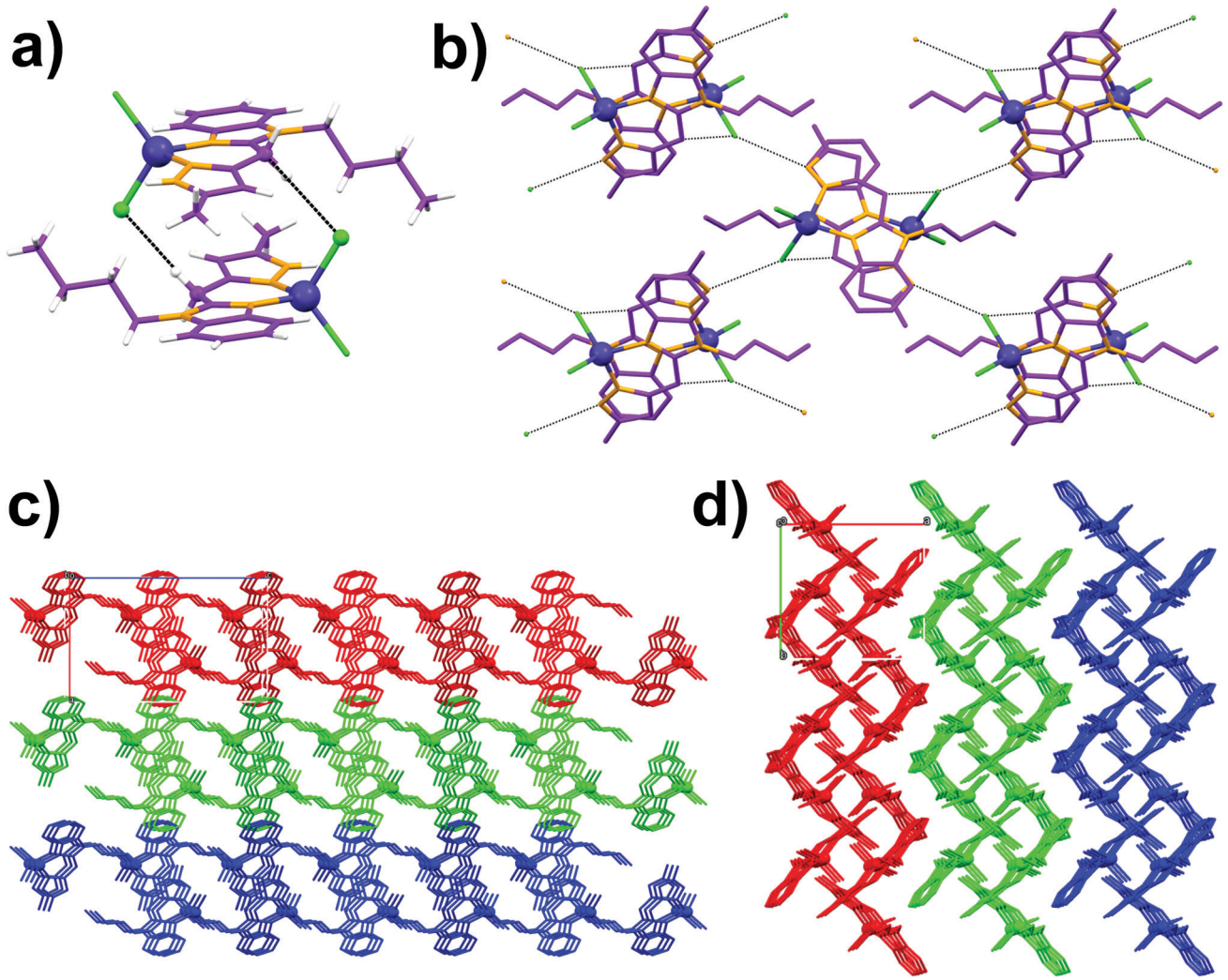

Fig. 2 Crystal structure illustration of **C1**, (a) 0D hydrogen bonded macrocycle, and (b) extension of the 0D hydrogen bonded macrocycle to a 2D sheet. Parallel packing of the 2D hydrogen bonded sheets along crystallographic axis ('*b*' c) and ('*c*' d) (adjacent sheets are shown in red, green and blue colours).

C–H of the butyl chain with the chloride anion, and C–H of the $-CH_2-$ spacer and water molecule, respectively. Such hydrogen bonding resulted in a 1D hydrogen bonded chain. This chain further self-assembled though weak C–H–Cl interactions, which led to the formation of a pair of 1D chains. Such a pair of chains recognized each other by van der Waals interactions, which supports the inclusion of water molecules within the crystal lattice (Fig. 3 and Fig. S3, ESI†).

Crystal structure C3

We followed exactly the same reaction conditions as for **C1** to synthesize **C3**, except that we have used $ZnCl_2$ instead of $CoCl_2{\cdot}6H_2O$. The resultant colourless prism shaped single crystal was analyzed using SXRD. SXRD analysis revealed that the crystal belongs to the monoclinic centrosymmetric space group *C*2/*c*. In the asymmetric unit there were two crystallographically independent molecules of the Zn(II) coordination complex of **L**, and four chloride anions (two are coordinated to each Zn(II)). In the unit cell eight such units are present (a total of sixteen molecules together, $Z = 8$) and are symmetrically related by a centre of inversion, 2-fold screw axis, and glide planes (Fig. S4, ESI†). The Zn(II) metal centre exhibits distorted tetrahedral geometry [$\angle$N–Zn–N = 89.40(15)–91.29(15)°; $\angle$N–Zn–Cl = 106.51(13)–122.48(11)°; $\angle$Cl–Zn–Cl = 111.90(5)–121.28(7)°] in which the coordination sites are occupied by two chloride anions, and N atoms of imidazole and pyrazole of the ligand **L**. The ligand **L** showed nonplanar geometry, which is revealed from the torsion angle (28.92 and 31.47° for crystallographically independent complexes) between the planes of the imidazole and pyrazole functionalities. The N–H···Cl hydrogen bonding [N–H···Cl = 3.197(4)–3.293(4) Å, $\angle$N–H–Cl = 160–168°] between two crystallographically independent molecules of **C3**, involving the N–H of the pyrazole moiety and the chloride anion, resulted in a 0D hydrogen bonded macrocycle, which is the primary supramolecular synthon. Additionally, the bifurcated C–H···Cl hydrogen bonding [C–H···Cl = 3.770–3.773(6) Å, $\angle$C–H–Cl = 148–166°] supported by the C–H of the $-CH_2-$ spacer and *n*-butyl chain with the chloride anion led to the formation of

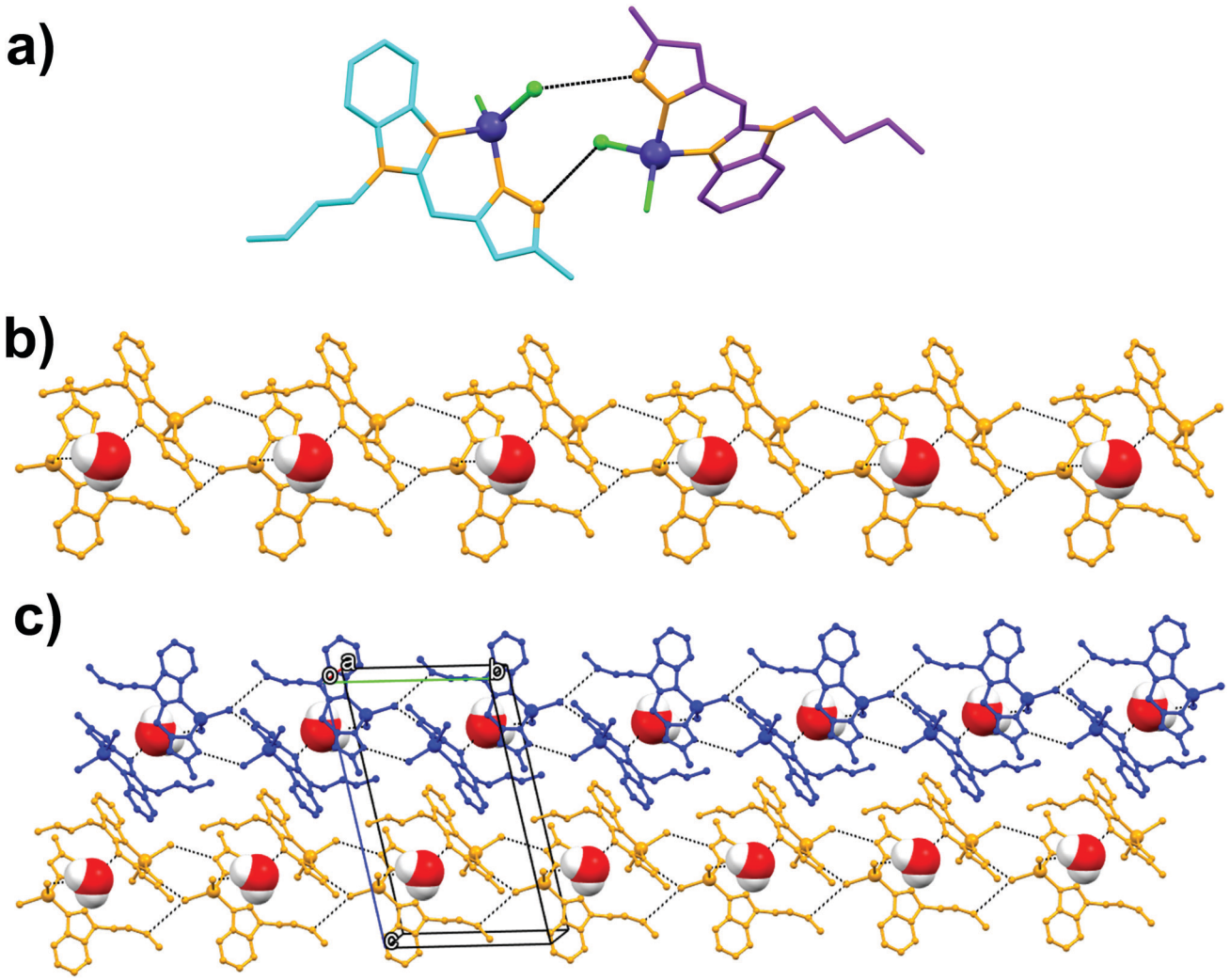

Fig. 3 Crystal structure illustration of **C2**, (a) 0D hydrogen bonded macrocycle, (b) 1D hydrogen bonded chain supported by various hydrogen bonding (shown in black colour dotted lines), involving the lattice included water molecule and moieties of the ligand and metal bound chloride, and (c) parallel packing of 1D hydrogen bonded chains (adjacent chains are shown in blue and orange colours, and the lattice included water molecule is shown in the space fill model).

a 1D hydrogen bonded chain. 1D chains are self-assembled into a pair of 1D chains, supported by π···π stacking involving the imidazole rings (3.376 Å) and C–H···Cl [C–H···Cl = 3.782(6) Å, ∠C–H–Cl = 150.63°] interactions. Interestingly this chain did not extend into a 2D sheet. Instead another set of 1D chains were found to be packed in an orthogonal fashion *via* C–H···π (3.589–3.614 Å) interactions involving the C–H of the *n*-butyl side chain and imidazole ring (Fig. 4).

FT-IR spectroscopy

Solid state Fourier transform infrared (FT-IR) analyses of **L** and its metal complexes **C1**, **C2** and **C3** were performed using an attenuated total reflection (ATR) device. ATR-FT-IR spectra were recorded from 4000 to 400 cm^{-1}. An overlay of the IR spectra of **L**, **C1**, **C2** and **C3** is illustrated in Fig. S5–S7 (ESI†). The ligand contains several binding sites which may coordinate to the metal ions. To assign the IR bands, the ligand spectrum was carefully compared with that of the complexes. The bands at 3190 cm^{-1} and at 3085 cm^{-1} were assigned to the stretching vibrations of N–H groups and aromatic C–H, respectively. The bands between 2861 and 2965 cm^{-1} were assigned to the symmetrical and asymmetric stretching vibrations of CH_3 and CH_2, respectively. The bands appearing at 1641 and 1615 cm^{-1} were assigned to the ν(C=N) imine group of pyrazole and benzimidazole rings, respectively. The comparison of the IR spectra of the ligand and its metal chelates indicated that the ligand was coordinated in a bidentate fashion. The bands detected at 1641 and 1615 cm^{-1} assigned to the ν(C=N) imine group vibrations of pyrazole and benzimidazole rings shifted down by 5–15 cm^{-1} indicating the participation of the pyrazole and benzimidazole ring nitrogen in chelation.[38,39] Further conclusive evidence of the coordination of this ligand with the metals was shown by the appearance of weak low frequency new bands in the 410–455 cm^{-1} region, which may probably be due to the formation of an M–N bond.[40,41] These new bands were observable only in the spectra of the metal complexes and

 This journal is © The Royal Society of Chemistry and the Centre National de la Recherche Scientifique 2020

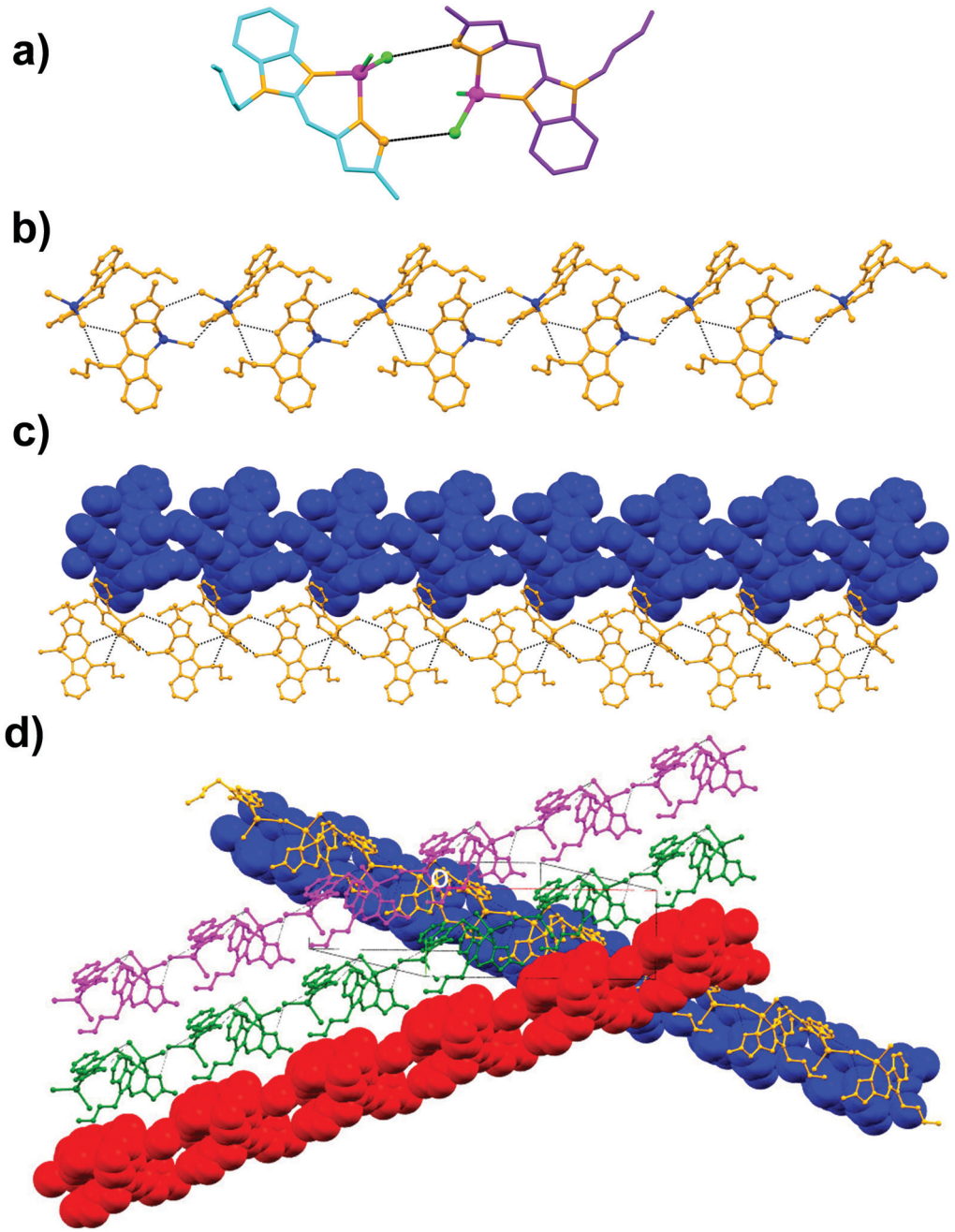

Fig. 4 Crystal structure illustration of **C3**, (a) 0D hydrogen bonded macrocycle, (b) 1D hydrogen bonded chain sustained by N–H···Cl and C–H···Cl hydrogen bonding (shown in black colour dotted lines), (c) parallel packing of a pair of 1D chains (adjacent chains are shown in blue and orange colours), and (d) orthogonal packing of a 2D hydrogen bonded sheet (formed by the self-assembly of 1D chains (adjacent chains are shown in red, green and magenta)) and a pair of 1D chains.

not in the spectra of the ligand, thus confirming the participation of the N heteroatom in the coordination. The FT-IR spectra of **C2** exhibit a broad band at ~3250–3500 cm^{-1}, which supports the presence of lattice water molecules, which was confirmed in our single X-ray diffraction study.

UV-visible spectroscopy

Spectrophotometric data were recorded at room temperature in the 200–900 nm range using DMSO as a solvent (Fig. S8, ESI†). The UV-vis spectra of **L** showed three absorption bands, two at λ_{max} = 280 nm and 305 nm, assigned to the π–π* of the aromatic rings, and a weak and broad band around λ_{max} = 345 nm, assigned to n–π* of the C═N groups. In the electronic absorption of the complexes, the absorption band found at λ_{max} = 280 nm is also present, being much narrower for **C3**. The UV-vis spectra of the complexes show the disappearance of the absorption band at λ_{max} = 305 nm observed in the ligand (**L**).

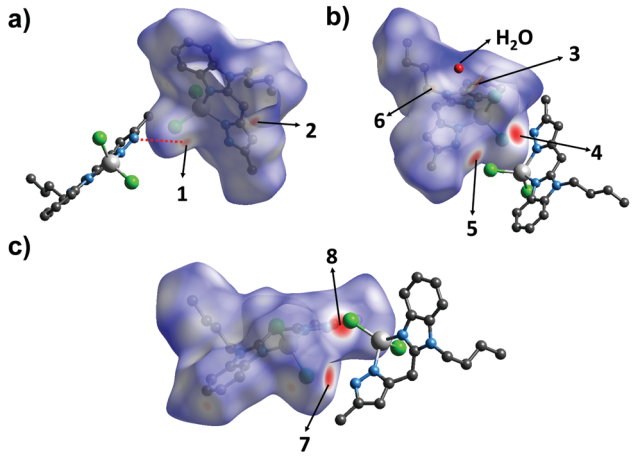

Fig. 5 Views of the d_{norm} Hirshfeld surfaces of **C1** (a), **C2** (b), and **C3** (c). The numbered arrows represent various hydrogen bonding interactions (1, 4, 5 and 7 are N–H···Cl; 2 and 8 are C–H···Cl; 6 is C–H···O; and 3 is O–H···Cl).

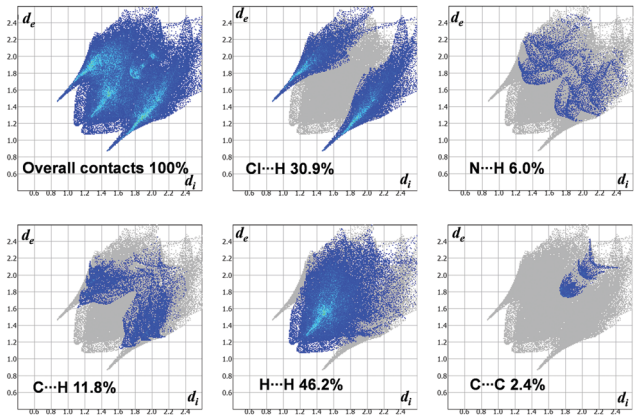

Fig. 6 2D Fingerprint plots derived from the Hirshfeld surfaces displaying various intermolecular interactions for C1.

Hirshfeld surface analysis

The supramolecular structures of the coordination complexes **C1**, **C2** and **C3** result from various hydrogen bonding interactions such as N–H···Cl, O–H···Cl, C–H···Cl, and C–H···O. Such interactions can be explored by using Hirshfeld surface analysis.[42] The Hirshfeld surfaces and their respective 2D fingerprint plots were calculated using CRYSTAL EXPLORER.[43] The Hirshfeld surfaces of the coordination complexes **C1**, **C2** and **C3** are shown in Fig. 5, displaying the surface map over the normalized contact distance (d_{norm}). This distance can be calculated from d_e (the distance between the Hirshfeld surface and adjacent molecule), d_i (the distance between the Hirshfeld surface and inside the molecule) and the van der Waals radii of the atoms (r_i^{vdW} or r_e^{vdW}), as follows:

$$d_{norm} = \frac{d_{i-}r_i^{vdW}}{r_i^{vdW}} + \frac{d_{e-}r_e^{vdW}}{r_e^{vdW}}$$

From the d_{norm} value, one can determine the regions participating in the intermolecular interactions in the complexes.

The Hirshfeld surfaces in d_{norm} of **C1**, **C2** and **C3** are spotted with red colour, indicating strong proximity, which corroborates well with the existing hydrogen bonding in **C1** (N–H···Cl, C–H···Cl), **C2** (N–H···Cl, O–H···Cl, C–H···Cl, C–H···O), and **C3** (N–H···Cl, C–H···Cl). The white and blue colours on the Hirshfeld surfaces of the coordination complexes indicate intermediate interactions and no supramolecular interactions, respectively. Similarly the red concave surface surrounded by receptors and the blue convex surface surrounding receptors on the Hirshfeld surfaces in the shape index of the coordination complexes further confirm the presence of such hydrogen bonding (Fig. S9, ESI†).

The 2D fingerprint plots further revealed the quantification (percentage contribution) of various supramolecular contacts, which correspond to the Cl···H, N···H, C···H, H···H, and C···C interactions from the Hirshfeld surface of the coordination compounds in **C1**, **C2** and **C3** (Fig. 6 and Fig. S10, S11, ESI†). From this plot, the contributions of the interatomic contacts to the Hirshfeld surfaces are Cl···H (30.9%), N···H (6.0%), C···H (11.8%), and H···H (46.2%) for **C1**, Cl···H (27.3%), N···H (6.1%), C···H (13.7%), and H···H (47.8%) for **C2**, and Cl···H (30.9%), N···H (7.4%), C···H (13.2%), and H···H (44.1%) for **C3**. Moreover, in all three complexes, there are two sharp spikes in the lower left area of the fingerprint plot, which represent the strong N–H···Cl hydrogen bonding ($d_i + d_e$ = 2.33–3.02 Å, 2.23–3.08 Å, and 2.22–2.90 Å, for **C1**, **C2**, and **C3** respectively, after considering both the Cl···H and N···H fingerprint plot); and C–H···Cl interactions ($d_i + d_e$ = 2.72–2.76 Å, 2.92–2.93 Å, and 2.76–2.85 Å, for **C1**, **C2**, and **C3** respectively). The contribution of C···C to the Hirshfeld surfaces is 2.4% (**C1**), 2.6% (**C2**), and 2.1% (**C3**), indicating the presence of C–H···π and/or π–π interactions.

Antibacterial activity

The antibacterial activities of the synthesized molecules (**3**, **4** and **L**) and metal complexes (**C1**, **C2** and **C3**) were tested against *E. coli* and *P. aeruginosa* as Gram-negative and *S. aureus* as Gram-positive microorganisms. The results were compared with chloramphenicol as a standard, at various concentrations.

The minimum inhibitory concentration (MIC) of **3**, **4** and **L** and the metal complexes has been evaluated. This concentration corresponds to the minimum concentration that inhibits the microorganism's growth: the lower it is, the higher the compound's antibacterial activity. The three complexes have higher antibacterial activities against *S. aureus* and *E. coli*. when compared to **3** and **4**, whereas **C1** and **C2** have higher activity against the free ligand (**L**) (Table 2). Complexes **C1** and **C2** have indeed

Table 2 MIC of the synthesized compounds against growth of bacteria (μg mL^{-1})

Compound	*S. aureus*	*E. coli*	*P. aeruginosa*
3	25	25	50
4	25	50	50
L	12.5	50	50
C1	6.25	25	50
C2	6.25	6.25	50
C3	12.5	12.5	50
Chloramphenicol	12.5	6.25	6.25

 This journal is © The Royal Society of Chemistry and the Centre National de la Recherche Scientifique 2020

outstanding activity against *S. aureus*, with an MIC value of 6.25 μg mL^{-1}, even better than the effect of chloramphenicol, an antibiotic, *e.g.* for the treatment of eye infections.[44] Complex **C2** displays strong activity against *E. coli*, with an MIC value of 6.25 μg mL^{-1}, which is comparable to the one of chloramphenicol. Complex **C3** displayed high activity against *S. aureus* and *E. coli*, with an MIC value of 12.5 μg mL^{-1}. Complexes **C1**, **C2** and **C3** have medium activity against *P. aeruginosa*, with an MIC value of 50 μg mL^{-1}, identical to the one of **L** and **3** and **4**.

These results show that the active complexes show, overall, higher antibacterial properties than the ligand, complex **C2** being the most active. Such increased activity of the complexes can be explained on the basis of Overtone's concept on cell permeability,[45] and Tweedy's chelation theory.[46] According to Overtone, the lipid membrane that surrounds the cell only favours the transition of lipid soluble materials, which controls the antifungal activity. On chelation, the polarity of the metal ion will be reduced to a greater extent due to the overlap of the ligand orbital and partial sharing of the positive charge of the metal ion with donor groups. Further, it increases the delocalization of π-electrons over the whole chelate ring and enhances the lipophilicity of the complexes. This increased lipophilicity enhances the penetration of the complexes into the lipid membrane and restricts further multiplicity of the microorganisms. In addition, the variation of the antimicrobial activities of the metal complexes against different bacteria depends on the impermeability of the cell or differences in the ribosomes in the microbial cells.

Discussion

Owing to the wide range of applications, crystal engineering of coordination complexes[47,48] and coordination polymers[49,50] has gained immense attention within the materials chemistry communities, in particular, compounds displaying pseudopolymorphism,[51] due to their use in the pharmaceutical industry and as a model for gas molecule adsorption.[52] Pseudopolymorphism is characterized by an identical chemical content crystallized with a different quantity or types of solvent molecules, and showing differences in crystal packing. It is important to study various factors responsible for the formation of pseudopolymorphs, since the bulk properties of crystalline materials basically depend upon their crystal contents, non-covalent interactions and supramolecular structures.[53] Among the various methods to control the formation of pseudopolymorphs through different parameters such as temperature, pH, various techniques of crystal growth *etc.*,[54] the nature of the solvent molecule (used for the crystallization of the compounds) is crucial. The solvent is responsible for the final crystal products in many ways, such as the crystal polymorph, crystal size, and morphology.[55] Thus, it is significant to study the effect of the solvent, which leads to pseudopolymorphs in coordination complexes. Such study is necessary to achieve more insights in the crystal engineering of molecules, and hence is beneficial to create the desired supramolecular structure, highly relevant for instance in pharmaceutical chemistry.

In the present work, we have used EtOH, EtOH and H_2O (1 : 1 v/v) as solvents to induce the formation of pseudopolymorphs **C1** (monoclinic, $P2_1/c$) and **C2** (triclinic, $P\bar{1}$). Both **C1** and **C2** were crystallized from exactly the same amounts of precursor materials (a 1 : 1 molar ratio of **L** and $CoCl_2{\cdot}6H_2O$) and at the same concentrations. The only difference is the solvent used for crystallization. While **C1** crystallizes with only one molecule in its asymmetric unit, **C2** crystallizes with two molecules of the complex and one molecule of water. Thus, the water molecule acted as a template for the formation of **C2**. Two additional hydrogen bonding interactions O–H···Cl and C–H···O are therefore present in the crystal structure of **C2**. Along with other interactions N–H···Cl and C–H···Cl, **C2** showed a 2D corrugated hydrogen bonded sheet with inclusion of a water molecule. On the other hand, the reaction conditions for the synthesis of **C3** were exactly the same as for **C1**, the only difference is the metal salt precursor ($ZnCl_2$); the resultant crystals (monoclinic, $C2/c$) of **C3** contain two molecules of the complex without any co-crystallization with a solvent molecule. Thus, the metal salt precursor induces the formation of **C3**. Moreover, the N–H···Cl and C–H···Cl hydrogen bonding in the crystal structure of **C1** and **C3** resulted in the formation of their supramolecular structure: a 2D hydrogen bonded sheet in **C1** and an orthogonally packed 2D sheet with a pair of 1D chains in **C3**. The difference in the packing of **C1**–**C3** is due to the difference in the crystal system and space groups. Such a difference is apparently influenced by the crystallization solvents and metal salt precursors. A molecular overlay diagram for **C1** and **C2** with the metal centre, nitrogen atoms of the benzimidazole and pyrazole rings associated with the tetrahedral coordination, and neighboring carbon atoms to these metal bound nitrogen atoms is shown in Fig. 7, which displays the difference in the torsion angle between the aromatic rings.

The crystal engineering of new materials, apart from the ordering of the chemical components in the lattice, aims to address the crystal structure–functional property correlation, in various fields of investigation. In the medicinal and health care sectors, the control of antibacterial properties represents a

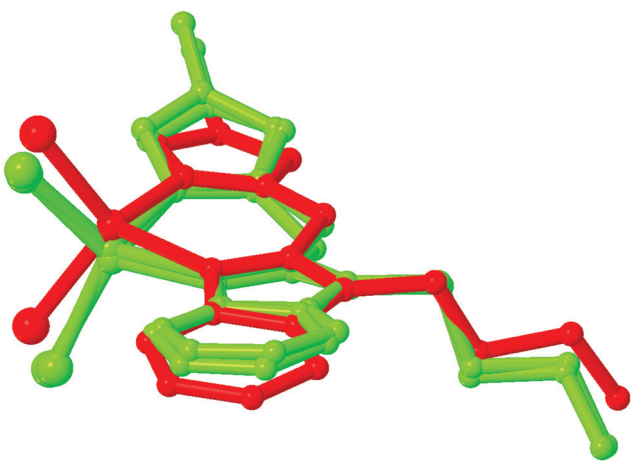

Fig. 7 A molecular overlay of the [Co**L**]Cl_2 unit from the pseudopolymorphs **C1** (red) and **C2** (green), with the Co(II), metal bound N atoms and their adjacent C atoms of the ligand L as the common basis. Note: There are two [Co**L**]Cl_2 molecular units in the asymmetric unit of **C2**.

current challenge in molecular science, given the increased resistance of antibiotics and virus propagation. The inspiration behind the present study stems from an intriguing observation which was made between antibacterial activity and bioactive molecules having crystal lattice included water molecules.[56] Indeed, the cell wall of bacteria is hydrophilic in nature, so that antibacterial crystalline compounds having lattice included water molecules are capable of showing more penetrability into the cell wall of bacteria and finally destroying them. Among the variety of molecules, azole ligands are potential candidates for antibacterial activity since they can act as an inhibitor of enoyl acyl carrier protein reductase (FabI), a protein that is involved in fatty acid synthesis in bacteria.[57] Secondly, coordination complexes of azole ligands were shown to display higher antimicrobial activity than that of free azole ligands.[58–65]

Thirdly, azole molecules display good solubility, biocompatibility and capability to interact with DNA of bacteria, through intermolecular interactions.[66] In addition, there are several examples of coordination compounds with azole ligands which host water molecule inclusion within their interstitial space.[49,67–69] Thus, stimulated by these aspects, we designed a new azole molecule, namely pyrazolyl-benzimidazole (**L**), to work as a ligand of Co(II) and Zn(II) coordination complexes. The synthesis was carried out with $CoCl_2{\cdot}6H_2O$ or $ZnCl_2$ with and without using water as a solvent, to afford three coordination complexes (**C1**, **C2** and **C3**). We deliberately used water for the synthesis of **C2**, and avoided water in the reaction medium for the synthesis of **C1** and **C3**, to make molecular crystalline solids with (**C2**) and without (**C1** and **C3**) lattice included water molecules, and further study their antibacterial capability. Remarkably, **C2** has shown greater antibacterial activity against both Gram-positive (*S. aureus*) and Gram-negative (*E. coli*) bacteria, compared to **C1**, **C3** and other reported Co(II) and Zn(II) complexes (Tables 2 and 3).

The presence of water molecules in the crystal lattice assisted the coordination complex **C2** to cross the cell wall of the bacteria more prominently than **C1** and **C3**.

The remarkable antibacterial activity of the **C1–C3** complexes could be due to the coordination of the metal with the condensed ring system, thus increasing the delocalization of the π electrons throughout the chelated ring and improving the lipophilicity of the complexes and thus the penetration of the complexes into the lipid membrane and further limiting the multiplicity of microorganisms. To our knowledge, the **C1–C3** complexes are among the most active complexes described in the literature, among Zn(II) and Co(II) complexes (Table 3). Other metal ions can display superior characteristics, *e.g.* $[Cd(HL)_2]$ and $[Cu_2(HL)_2(OAc)_2]$ (H_2L = hydrazinyl-(pyridin-2-yl)salicyladimine), which display normalized MIC = 5 and 7 μg mL^{-1}, respectively.[71]

Table 3 Antibacterial activity of **C1**, **C2**, **C3** and other model complexes

Metal complexes	Antibacterial activity (MIC in μg mL^{-1})			Ref.
	S. aureus	*E. coli*	*P. aeruginosa*	
C1	6.25	25	50	This work
C2	6.25	6.25	50	This work
C3	12.5	12.5	50	This work
$[Zn(nap)_2(dap)]^a$	56.25	225	225	70
$[Zn(HL)_2]^b$	700	600	—	71
$[Co(HL)_2]Cl{\cdot}CH_3OH^b$	400	40	—	71
$[Zn(nobpy)]CF_3SO_3{}^c$	750	750	>3000	72
$[Zn(cobpy)]CF_3SO_3{}^c$	750	750	750	72
$[CoL_2]^d$	625	500	—	73
$[ZnL_2]^d$	125	125	—	73
$[Co(chysa)Cl_2]^e$	16	128	128	74
$[Co(chysa)(CH_3COO)_2]^e$	32	64	64	74
$[Zn_4LCl_2(H_2O)_6]^f$	20	16	—	75
$[Co(diasa)Cl_2]^g$	64	128	64	76
$[Co(diasa)(NO_3)_2]^g$	128	>128	>128	76
$[Co(diasa)(OAc)_2]^g$	>128	>128	NA	76

[a] nap = naproxen. dap = 1,3-diaminopropane. [b] H_2L = hydrazinyl-(pyridin-2-yl)salicyladimine. [c] nobpy = 5-nitro-(8-oxyquinoline)-2′2-bipyridine. cobpy = 5-chloro-(8-oxyquinoline)-2′2-bipyridine. [d] HL = 2-((*E*)-(2-methoxyphenylimino)-methyl)-4-bromophenol. [e] chysa = Schiff base synthesized from carbohydrazide and isatin. [f] LH_6 = 4,4′-bis(2′,4′-dihydroxy-5′carboxyphenylazo)-diphenylether. [g] diasa = Schiff base synthesized from 2,6-diaminopyridine and isatin.

Experimental

Syntheses

Chemical reagents were purchased from Fluka and Sigma-Aldrich chemicals.

(*Z*)-4-(2-Oxopropylidene)-4,5-dihydro-1,5-benzodiazepin-2(3*H*)-one (3). Dehydroacetic acid (0.02 mol, 3.36 g) and *o*-phenylenediamine (0.04 mol, 4.32 g) were refluxed in xylene (80 mL) for 4 h. A precipitate was obtained, filtered and then recrystallized from ethanol as a yellow solid. Yield: 75% (3.24 g); M.p. (°C): 236–238; IR (ATR, ν (cm^{-1})): 1671, 1607 (C═O), 1575 (C═C); ^{1}H NMR (400 MHz, DMSO-d^6, δ (ppm)): 2.00 (s, 3H, CH3); 3.00 (s, 2H, CH2); 5.20 (s, 1H); 7.10 (m, 4H); ESI-MS (MeOH): m/z = 217 $[M + H]^+$.

(4*Z*)-1-Butyl-4-(2-oxopropylidene)-2,3,4,5-tetrahydro-1*H*-1,5-benzodiazepin-2-one (4). To a solution of (*Z*)-4-(2-oxopropylidene)-4,5-dihydro-1,5-benzodiazepin-2(3*H*)-one (2.38 mmol; 510 mg) in dichloromethane (15 mL) were added 1.5 eq. (0.4 mL) of 1-bromobutane, (3.57 mmol; 98 mg) of potassium hydroxide dissolved in water and 0.23 mmol (74 mg) of tetra-*n*-butyl ammonium bromide (TBAB). The mixture was kept under magnetic stirring at room temperature for 48 h. 5 mL of water was added and then the organic phase was extracted, dried and concentrated under reduced pressure. The residue obtained was chromatographed on a column of silica gel (hexane/ethyl acetate 8/2) to give a white solid. Yield: 77% (499 mg). M.p. (°C): 134–136 (hexane/ethyl acetate 8 : 2); IR (ATR, ν (cm^{-1})): 3193 (N–H), 1671, 1621 (C═O), 1389–1299 (C–N); ^{1}H NMR (DMSO-d_6) δ ppm: 0.74 (t, 3H, CH_3–CH_2, J = 7.5 Hz); 1.07 (m, 2H, CH_3–CH_2–CH_2); 1.27 (m, 2H, CH_2–CH_2–CH_2); 2.04 (s, 3H, CH_3–CO); 2.96 (AB, 2H, CH_2); 3.61 (m, 2H, N–CH_2); 5.36 (s, 1H, CH–CO); 7.25–7.52 (m, 4H, CH_{ar}); 12.13 (s, ^{1}H, NH); ^{13}C NMR (DMSO-d_6) δ ppm: 13.40 (CH_3–CH_2); 19.02 (CH_2–CH_2–CH_3); 29.10 (CH_3–CO); 29.36 (CH_2–CH_2–CH_2); 40.92 (N–CH_2); 46.49 (CH_2 diazépine); 95.80 (═CH); 122.93–126.26 (CH_{ar}); 132.79–133.84 (Cq ar); 156.20 (NH–Cq); 166.39 (N–CO); 196.66 (CO–CH_3). ESI-MS (MeOH): m/z = 273.2 $[M + H]^+$, 295.2 $[M + Na]^+$.

 This journal is © The Royal Society of Chemistry and the Centre National de la Recherche Scientifique 2020

1-*n*-Butyl-2-((5-methyl-1*H*-pyrazol-3-yl)methyl)-1*H*-benzimidazole (L). To a solution (2.6 mmol, 0.7 g) of 1-butyl-4-(2-oxopropylidene)-4,5-dihydro-1*H*-1,5-benzodiazepin-2(3*H*)-one in ethanol (15 mL) was slowly added hydrazine monohydrate (10.3 mmol, 0.5 mL). The reaction mixture was refluxed for 2 h. After cooling, the solution was concentrated to dryness. The residue was washed with absolute ethanol (10 mL) and a yellow solid was collected by filtration, and dried in air. Yield: 98% (0.68 g); M.p. (°C): 115–117 °C (EtOH); IR (ATR, ν (cm^{-1})): 3190 (N–H), 2861–2965 (CH_3, CH_2), 1641 (C═N), 1615 (C═N); ^{1}H NMR ($CDCl_3$) δ ppm: 0.83 (t, 3H, CH_3–C_3H_6, J = 7.5 Hz); 1.26 (m, 2H, CH_2–CH_2–CH_3); 1.50 (m, 2H, CH_2–CH_2–CH_2); 2.13 (s, 3H, CH_3–pyraz.); 3.17 (m, 2H, N–CH_2); 4.17 (s, 2H, benzim. –$CH_{2pyraz.}$); 5.80 (s, 1H, $CH_{pyraz.}$); 6.56–7.54 (m, 4H, H_{ar}); 12.28 (s, ^{1}H, NH); ^{13}C NMR ($CDCl_3$) δ ppm: 13.58 (CH_3–C_3H_6), 19.47 ($CH_{3\text{-}pyraz.}$), 29.40 (CH_2–CH_2–CH_3), 31.22 (benzim. –CH_2–$_{pyraz.}$), 42.92 (CH_2–CH_2–CH_2), 46.01 (N–CH_2), 103.09 ($CH_{pyraz.}$), 109.97–121.11 (CH_{ar}), 128.69–129.56 (Cq_{ar}), 135.18 (Cq═$N_{pyraz.}$), 142.26 (Cq–NH), 144.78 (N–Cq═N); ESI-MS (MeOH): m/z = 269.7 $[M + H]^+$, 291.0 $[M + Na]^+$. UV/Vis (DMSO): λ_{max} = 280, 305, 345 nm.

[CoL]·Cl_2 (C1). $CoCl_2{\cdot}6H_2O$ (0.07 mmol; 17 mg) was dissolved in ethanol (5 mL) and added to a solution of L (0.07 mmol; 19 mg) in ethanol (5 mL). The resulting light blue solution was left at room temperature. Blue single crystals were obtained by slow evaporation of a clear blue clear solution of the reaction mixture after 24 h. Yield: 48% (13 mg). IR (ATR, ν (cm^{-1})): 3208 (N–H), 2868–2966 (CH_3, CH_2), 1657 (C═N), 1567 (C═N); UV/Vis (DMSO, λ_{max} (nm)): 280, 327; ESI-MS (MeOH): m/z = 594.7, 595.5 $[2L + Co]^+$, 538.4 $[2L - C_4H_9]^+$, 269.7 $[L + H]^+$.

[Co_2L_2]Cl_2·H_2O (C2). $CoCl_2{\cdot}6H_2O$ (0.07 mmol; 17 mg) was dissolved in water (5 mL) and added to a solution of L (0.07 mmol; 19 mg) in ethanol (5 mL). The resulting light blue solution was left at room temperature. Blue single crystals were obtained by slow evaporation of a clear blue clear solution of the reaction mixture after 24 h. Yield: 54% (31 mg). IR (ATR, ν (cm^{-1})): 3250–3500 (OH), 3127 (N–H), 2854–2972 (CH_3, CH_2), 1631 (C═N), 1568 (C═N); UV/vis (DMSO): λ_{max} = 280, 327 nm; ESI-MS (MeOH): m/z = 594.7, 595.5 $[2L + Co]^+$, 538.4 $[2L - C_4H_9]^+$, 269.7 $[L + H]^+$.

[Zn_2L_2]Cl_2 (C3). $ZnCl_2$ (0.07 mmol, 10 mg) was dissolved in ethanol (5 mL) and added to a solution of L (0.07 mmol; 19 mg) in ethanol (5 mL). The resulting light yellow solution was left at room temperature. Yellow single crystals were obtained by slow evaporation of the reaction mixture after 24 h. Yield: 64% (31 mg). IR (ATR, ν (cm^{-1})): 3194 (N–H), 2856–2959 (CH_3, CH_2), 1615 (C═N), 1575 (C═N); UV/vis (DMSO): λ_{max} = 280 nm; ESI-MS (MeOH): m/z = 599.3, 602.7 $[2L + Zn]^+$, 543.3 $[2L - C_4H_9]^+$, 269.7 $[L + H]^+$.

Characterization methods

Melting points were measured using a Buchi B-545 digital capillary melting point apparatus and used without correction. Reactions were checked with TLC using aluminium sheets using silica gel 60 F254 from Merck. IR spectra were recorded on a PerkinElmer VERTEX 70 FT-IR spectrometer covering the range 400–4000 cm^{-1}. ^{1}H and ^{13}C NMR spectra were recorded in DMSO-d_6 and $CDCl_3$ on a Bruker spectrometer (400 MHz). Chemical shifts are expressed in ppm by using tetramethylsilane (TMS) as an internal reference. Mass spectra were collected in MeOH using an API 3200 LC/MS/MS system, equipped with an ESI source. UV/vis measurements were carried out on a Lambda 35 ES UV/vis spectrophotometer (PerkinElmer, Waltham, MA, USA) in the range of 200–900 nm.

Single crystal X-ray analysis

X-ray single crystal data were collected by using MoK_α (λ = 0.71073 Å) radiation on a STOE IPDS 2 diffractometer equipped with an STOE image plate (34 cm diameter) area detector, and a 2-circle goniometer. Data collection, data reduction, and structure solution/refinement were carried out using the software package X-RED32; Stoe & Cie, 2002. All structures were solved by direct methods and refined in a routine manner (SHELXL).[77] In most of the cases, non-hydrogen atoms were treated anisotropically. Whenever possible, the hydrogen atoms were located on a difference Fourier map and refined. In other cases, the hydrogen atoms were geometrically fixed. Molecular graphics were generated by using MERCURY 3.9[78] and POV-Ray software. The details of the X-ray crystal data and the structure solution as well as the refinement are given in Table 1. CCDC 1895214, 1959576 and 1895673 for **C1**, **C2**, and **C3** respectively.†

Hirshfeld surface analysis

The Hirshfeld surfaces of the coordination complexes and the corresponding 2D fingerprint plots were obtained by using the software package CRYSTAL EXPLORER 17.5.43 *d*-plot is used to measure the distances to the surface from nuclei outside (d_e) and inside (d_i) the Hirshfeld surface. The d_{norm} surface is plotted over a fixed colour scale of −0.25 a.u. (red) to −0.95 a.u. (blue). The shape index plot is mapped in the colour range −1.0 a.u. (concave) to 1.0 a.u. (convex) and the curvedness plot in the range of −4.0 a.u. (flat) to −0.4 (singular). The 2D fingerprint plots were displayed in the 0.5–2.8 Å range, including reciprocal contacts.

Antibacterial activity

Compounds were evaluated for their *in vitro* antibacterial activity against *Escherichia coli* ATCC4157, *Pseudomonas aeroginosa* ATCC 27853 and *Staphylococcus aureus* ATCC 25923 delivered from the Department of Microbiology Medicinal, National Institute of Hygiene, Rabat, Morocco. The agar dilution method[79] was performed using Mueller–Hinton agar (Hi-media) plates (37 °C, 24 h). Suspensions of each microorganism were prepared to contain approximately 106 colony forming units (CFU) and applied to plates with serially diluted compounds to be tested and incubated at 37 °C overnight. The minimum inhibitory concentration (MIC) was considered to be the lowest concentration that completely inhibited the growth on agar plates, disregarding a single colony or faint haze caused by the inoculum.

Conclusions

Mononuclear Co(II) complexes (**C1** and **C2**) and a Zn(II) complex (**C3**) were built from a new pyrazolyl-benzimidazole ligand. Their single crystal X-ray diffraction analysis revealed that their

coordination or hydrogen bonding dimensionality plays an important role for the formation of the supramolecular structure. The self-assembly of **C1** and **C3** *via* N–H···Cl and C–H···Cl hydrogen bonding led to a 2D hydrogen bonded sheet and an orthogonally packed [2D sheet + a pair of 1D chains] supramolecular structure, respectively. On the other hand, in **C2** there are more supramolecular interactions such as N–H···Cl, C–H···Cl, O–H···Cl, and C–H···O, which resulted in a 2D corrugated hydrogen bonded sheet with inclusion of a water molecule. Hirshfeld surface analysis confirmed the presence of various hydrogen bonding and π···π stacking interactions. Noticeable antibacterial activity against the strains of bacteria was revealed for these complexes. Remarkably, the best result was shown by **C2** (normalized MIC = 6.25 μg mL^{-1}), and this correlated well with the crystal structure (containing a lattice included water molecule, which is one of the key factors for crystalline anti-bacterial agents). Thus, the study described herein clearly supports the proof of concept based on which these antibacterial agents were designed. We anticipate that the present study will open a new crystal engineering route for the design and synthesis of new antibacterial agents.

Abbreviations

DHA	Dehydroacetic acid
ESI-MS	Electrospray ionization-mass spectrometry
EtOH	Ethanol
IR	Infrared spectrophotometry
NMR	Nuclear magnetic resonance spectroscopy

Conflicts of interest

There are no conflicts to declare.

Acknowledgements

This work was supported by a bilateral WBI action with Morocco (COP 22 Program 2018-2022), the Fonds De La Recherche Scientifique – FNRS (PDR T.0102.15, CDR 33694457) and project No. PYOFEN.1906.19.001.

Notes and references

1 A. Singh, P. Raj, J. J. Dubowski and N. Singh, *Cryst. Growth Des.*, 2018, **18**, 4320–4333.
2 A. Garai and K. Biradha, *Cryst. Growth Des.*, 2019, **19**, 4602–4646.
3 P. Gütlich, A. B. Gaspar and Y. Garcia, *Beilstein J. Org. Chem.*, 2013, **9**, 342–391.
4 Y. Garcia, N. N. Adarsh and A. D. Naik, *Chimia*, 2013, **67**, 411–418.
5 Y. Boland, B. Tinant, D. A. Safin, J. Marchand-Brynaert, R. Clérac and Y. Garcia, *CrystEngComm*, 2012, **14**, 8153–8155.
6 W. L. Driessen, W. G. R. Wiesmeijer, M. Schipper-Zablotskaja, R. A. G. De Graaff and J. Reedijk, *Inorg. Chim. Acta*, 1989, **162**, 233–238.
7 C. Dowling, V. J. Murphy and G. Parkin, *Inorg. Chem.*, 1996, **35**, 2415–2420.
8 Y. Bansal and O. Silakari, *Bioorg. Med. Chem.*, 2012, **20**, 6208–6236.
9 K. Karrouchi, E. B. Yousfi, N. K. Sebbar, Y. Ramli, J. Taoufik, Y. Ouzidan, M. Ansar, Y. N. Mabkhot, H. A. Ghabbour and S. Radi, *Int. J. Mol. Sci.*, 2017, **18**, 2215.
10 K. Karrouchi, S. Radi, Y. Ramli, J. Taoufik, Y. N. Mabkhot, F. A. Al-aizari and M. Ansar, *Molecules*, 2018, **23**, 134.
11 R. R. Pillai, K. Karrouchi, S. Fettach, S. Armaković, S. J. Armaković, Y. Brik, J. Taoufik, S. Radi, M. E. Faouzi and M. H. Ansar, *J. Mol. Struct.*, 2019, **1177**, 47–54.
12 T. S. Reddy, H. Kulhari, V. G. Reddy, V. Bansal, A. Kamal and R. Shukla, *Eur. J. Med. Chem.*, 2015, **101**, 790–805.
13 X. Qiao, Z.-Y. Ma, J. Shao, W.-G. Bao, J.-Y. Xu, Z.-Y. Qiang and J.-S. Lou, *Biometals*, 2014, **27**, 155–172.
14 M. Boca, R. F. Jameson and W. Linert, *Coord. Chem. Rev.*, 2011, **255**, 290–317.
15 M. Devereux, D. O'Shea, H. O'Connor, H. Grehan, G. Connor, M. McCann, G. Rosair, F. Lyng, A. Kellett, M. Walsh, D. Egan and B. Thati, *Polyhedron*, 2007, **26**, 4073–4084.
16 M. Bouchouit, M. E. Said, M. Kara Ali, S. Bouacida, H. Merazig, H. Kacem Chaouche, A. Chibani, B. Zouchoune, A. Belfaitah and A. Bouraiou, *Polyhedron*, 2016, **119**, 248–259.
17 S. Tabassum, A. Asim, F. Arjmand, M. Afzal and V. Bagchi, *Eur. J. Med. Chem.*, 2012, **58**, 308–316.
18 M. X. Li, L. Z. Zhang, C. L. Chen, J. Y. Niu and B. S. Ji, *J. Inorg. Biochem.*, 2012, **106**, 117–125.
19 L. G. Lavrenova, T. A. Kuz'menko, A. D. Ivanova, A. I. Smolentsev, V. Y. Komarov, A. S. Bogomyakov, L. A. Sheludyakova and E. V. Vorontsova, *New J. Chem.*, 2017, **41**, 4341–4347.
20 J. G. Małecki, *Struct. Chem.*, 2012, **23**, 461–472.
21 A. Garai, S. Sasmal and K. Biradha, *Cryst. Growth Des.*, 2016, **16**, 4457–4466.
22 R. Saiki, H. Miyamoto, H. Sagayama, R. Kumai, G. N. Newton, T. Shiga and H. Oshio, *Dalton Trans.*, 2019, **48**, 3231–3236.
23 W. Ahmad, S. A. Khan, K. S. Munawar, A. Khalid and S. Kawanl, *Trop. J. Pharm. Res.*, 2017, **16**, 1137–1146.
24 P. P. Dholakiya and M. N. Patel, *Synth. React. Inorg. Met.-Org. Chem.*, 2004, **34**, 383–395.
25 L. Guo, C. Huang, L. Liu, Z. Shao, Y. Tong, H. Hou and Y. Fan, *Cryst. Growth Des.*, 2016, **16**, 4926–4933.
26 T. Shiga, R. Saiki, L. Akiyama, R. Kumai, D. Natke, F. Renz, J. M. Cameron, G. N. Newton and H. A. Oshio, *Angew. Chem., Int. Ed.*, 2019, **58**, 5658–5662.
27 A. D. Naik, K. Robeyns, C. F. Meunier, A. F. Léonard, A. Rotaru, B. Tinant, Y. Filinchuk, B. L. Su and Y. Garcia, *Inorg. Chem.*, 2014, **53**, 1263–1265.
28 K. Chkirate, N. K. Sebbar, K. Karrouchi and E. M. Essassi, *J. Maroc. Chim. Heterocycl.*, 2018, **17**, 1–27.
29 K. Chkirate, Y. El Bakri, E. M. Essassi and J. T. Mague, *IUCrData*, 2017, **2**, x170116.
30 F. Sbai, K. Chkirate, R. Regragui, E. M. Essassi and M. Pierrot, *Acta Crystallogr., Sect. E: Struct. Rep. Online*, 2002, **58**, m337–m339.
31 K. Chkirate, S. Fettach, K. Karrouchi, N. K. Sebbar, E. M. Essassi, J. T. Mague, S. Radi, M. E. A. Faouzi, N. N. Adarsh and Y. Garcia, *J. Inorg. Biochem.*, 2019, **191**, 21–28.

 This journal is © The Royal Society of Chemistry and the Centre National de la Recherche Scientifique 2020

32 K. Chkirate, S. Kansiz, K. Karrouchi, J. T. Mague, N. Dege and E. M. Essasi, *Acta Crystallogr., Sect. E: Struct. Rep. Online*, 2019, **75**, 154–158.

33 K. Chkirate, S. Kansiz, K. Karrouchi, J. T. Mague, N. Dege and E. M. Essasi, *Acta Crystallogr., Sect. E: Crystallogr. Commun.*, 2019, **75**, 33–37.

34 K. Chkirate, N. K. Sebbar, T. Hokelek, D. Krishnan, J. T. Mague and E. M. Essassi, *Acta Crystallogr., Sect. E: Crystallogr. Commun.*, 2018, **74**, 1669–1673.

35 K. Chkirate, R. Regragui, E. M. Essassi and M. Pierrot, *Z. Kristallogr. - New Cryst. Struct.*, 2001, **216**, 635–636.

36 M. El Abbassi, E. M. Essassi and J. Fifani, *Tetrahedron Lett.*, 1987, **28**, 1389–1392.

37 S. Hu, C. Ma, F. Zhan, Y. Cao, P. Hu and Q. Zhen, *Chem. Pap.*, 2017, **71**, 1323–1329.

38 K. Nakamoto, *Infrared and Raman Spectra of Inorganic and Coordination Compounds*, J. Wiley and Sons, New York, 4th edn, 1986.

39 P. Kalaivani, R. Prabhakaran, P. Poornima, F. Dallemer, K. Vijayalakshmi, V. Vijaya Padma and K. Natarajan, *Organometallics*, 2012, **31**, 8323–8332.

40 G. Kumaravel, P. P. Utthra and N. Raman, *Bioorg. Chem.*, 2018, **77**, 269–279.

41 A. Majumder, G. M. Rosair, A. Mallick, N. Chattopadhyay and S. Mitra, *Polyhedron*, 2006, **25**, 1753–1762.

42 H. L. Hirshfeld, *Theor. Chim. Acta*, 1977, **44**, 129–138.

43 M. J. Turner, J. J. McKinnon, S. K. Wolff, D. J. Grimwood, P. R. Spackman, D. Jayatilaka and M. A. Spackman, *CrystalExplorer17*, University of Western Australia, 2017.

44 L. Drago, *Microorganisms*, 2019, **7**, 278.

45 Y. Anjaneyula and R. P. Rao, *Synth. React. Inorg. Met.-Org. Chem.*, 1986, **16**, 257–272.

46 N. Dharmaraj, P. Viswanathamurthi and K. Natarajan, *Transition Met. Chem.*, 2001, **26**, 105–109.

47 A. Thakur, N. N. Adarsh, A. Chakraborty, M. Devi and S. Ghosh, *J. Organomet. Chem.*, 2010, **695**, 1059–1064.

48 N. N. Adarsh, D. K. Kumar and P. Dastidar, *Inorg. Chem. Commun.*, 2008, **11**, 636–642.

49 N. N. Adarsh, M. M. Dîrtu, A. D. Naik, A. F. Léonard, N. Campagnol, K. Robeyns, J. Snauwaert, J. Fransaer, B. L. Su and Y. Garcia, *Chem. – Eur. J.*, 2015, **21**, 4300–4307.

50 M. Paul, N. N. Adarsh and P. Dastidar, *Cryst. Growth Des.*, 2012, **12**, 4135–4143.

51 G. R. Desiraju, *Angew. Chem., Int. Ed.*, 2007, **46**, 8342.

52 X. Luo, L. Sun, J. Zhao, D.-S. Li, D. Wang, G. Li, Q. Huo and Y. Liu, *Cryst. Growth Des.*, 2015, **15**, 4901–4907.

53 J. M. Lehn, *Proc. Natl. Acad. Sci. U. S. A.*, 2002, **99**, 4763–4768.

54 D. Mangin, F. Puel and S. Veesler, *Org. Process Res. Dev.*, 2009, **13**, 1241–1253.

55 I. Weissbuch, V. Y. Torbeev, L. Leiserowitz and M. Lahav, *Angew. Chem., Int. Ed.*, 2005, **44**, 3226–3229.

56 A. Bijelic, M. Aureliano and A. Rompel, *Chem. Commun.*, 2018, **54**, 1153–1169.

57 V. S. Pore, M. A. Jagtap, S. G. Agalave, A. K. Pandey, M. I. Siddiqi, V. Kumar and P. K. Shukla, *Med. Chem. Commun.*, 2012, **3**, 484–488.

58 C. Xing, Q. Xu, H. Tang, L. Liu and S. Wang, *J. Am. Chem. Soc.*, 2009, **131**, 13117–13124.

59 K. Singh, Y. Kumar, P. Puri, M. Kumar and C. Sharma, *Eur. J. Med. Chem.*, 2012, **52**, 313.

60 S. Li, J.-X. Chen, Q.-X. Xiang, L.-Q. Zhang, C.-H. Zhou, J.-Q. Xie, L. Yu and F.-Z. Li, *Eur. J. Med. Chem.*, 2014, **84**, 677–686.

61 P. V. Simpson, C. Nagel, H. Bruhn and U. Schatzschneider, *Organometallics*, 2015, **34**, 3809–3815.

62 M. S. Al-Fakeh, *Org. J. Chem.*, 2016, **32**, 1155–1162.

63 K. F. Castillo, N. J. Bello-Vieda, N. G. Nunez-Dallos, H. F. Pastrana, A. M. Celis, S. Restrepo, J. J. Hurtado and A. G. Avila, *J. Braz. Chem. Soc.*, 2016, **27**, 2334–2347.

64 N. J. Bello-Vieda, H. F. Pastrana, M. F. Garavito, A. G. Avila, A. M. Celis, A. Munoz-Castro, S. Restrepo and J. J. Hurtado, *Molecules*, 2018, **23**, 361/1–361/17.

65 N. Amiri, M. Hajji, F. B. Taheur, S. Chevreux, T. Roisnel, G. Lemercier and H. Nasri, *J. Solid State Chem.*, 2018, **258**, 477–484.

66 X. Wang, Y. Du and H. Liu, *Carbohydr. Polym.*, 2004, **56**, 21–26.

67 A. D. Naik, M. M. Dîrtu, A. Léonard, B. Tinant, J. Marchand-Brynaert, B. L. Su and Y. Garcia, *Cryst. Growth Des.*, 2010, **10**, 1798–1807.

68 A. D. Naik, B. Tinant, A. Léonard, J. Marchand-Brynaert, B. L. Su and Y. Garcia, *Cryst. Growth Des.*, 2011, **11**, 4034–4043.

69 H. Benaissa, M. Wolff, K. Robeyns, G. Knör, K. Van Hecke, N. Campagnol, J. Fransaer and Y. Garcia, *Cryst. Growth Des.*, 2019, **19**, 5292–5307.

70 Y.-C. Chu, T.-T. Wang, L.-J. Wang, Q.-Y. Luo, R. Jia, T.-C. Hong, X.-M. Wang and H.-L. Zhu, *Polyhedron*, 2019, **163**, 71–76.

71 W. Cao, Y. Liu, T. Zhang and J. Jia, *Polyhedron*, 2018, **147**, 62–68.

72 C. D. S. Chagas, F. L. A. Fonseca and I. A. Bagatin, *Mater. Sci. Eng., C*, 2019, **98**, 1043–1052.

73 M. Galini, M. Salehi, M. Kubicki, A. Amiri and A. Khaleghian, *Inorg. Chim. Acta*, 2017, **461**, 167–173.

74 K. Kumar, M. Kamboj, K. Jain and D. P. Singh, *Spectrochim. Acta, Part A*, 2014, **128**, 243–247.

75 B. B. Mahapatra, S. Chaulia, A. K. Sarangi, S. Dehury and J. Panda, *J. Mol. Struct.*, 2015, **1087**, 11–25.

76 D. P. Singh, V. Malik, K. Kumar, C. Sharma and K. R. Aneja, *Spectrochim. Acta, Part A*, 2010, **76**, 45–49.

77 G. M. Sheldrick, *Acta Crystallogr., Sect. C: Struct. Chem.*, 2015, **71**, 3–8.

78 C. F. Macrae, P. R. Edgington, P. McCabe, E. Pidcock, G. P. Shields, R. Taylor, M. Towler and J. Van De Streek, *J. Appl. Crystallogr.*, 2006, **39**, 453–457.

79 A. T. Talbaoui, N. Jamaly, A. I. Idrissi, M. Bouksaim, S. Gmouh, M. El Moussaouiti, A. Benjouad and Y. Bakri, *J. Med. Plants Res.*, 2012, **6**, 4593–4600.